JOURNAL OF AIRCRAFT
Vol. 40, No. 6, November–December 2003

Feasibility Study of Constant Eddy-Viscosity Assumption in Gradient-Based Design Optimization

Chang Sung Kim,* Chongam Kim,† and Oh Hyun Rho‡
Seoul National University, Seoul 151-742, Republic of Korea

A feasibility study is carried out by investigating the effects of a usual assumption of constant turbulent eddy viscosity on the aerodynamic design using an adjoint variable method, one of the most efficient gradient-based optimization techniques. Accurate unsteady and steady flow analyses are followed by the aerodynamic sensitivity analysis for the Navier–Stokes equations coupled with two-equation turbulence models. A challengeable approach for high-lift design optimization at higher angles of attack is also proposed, which is based on unsteady sensitivity analysis using a dual time-stepping method and the chimera overset grid scheme. Through the comparison of the sensitivity gradients with respect to all of the design variables including angle of attack, it is observed that the constant turbulent eddy-viscosity assumption might provide inaccurate gradients in sensitivity analyses such as transonic airfoil with a strong shock and high-lift airfoil at a high angle of attack close to stall angle. Simultaneously, however, the final design results indicate that both approaches are acceptable in engineering applications. Both the single- and multi-element airfoil design optimizations using the constant eddy-viscosity assumption are carefully assessed in terms of design accuracy, computer memory overheads, and total design time in various design examples.

Introduction

As computational power advances, design optimization tools using computational fluid dynamics (CFD) have gradually played an important role in aerodynamic design process. Among advanced optimization techniques, the gradient-based optimization method has been widely used and applied even to multidisciplinary design optimization (MDO). In general, a gradient-based design optimization requires two steps. The first is to obtain the search direction that defines the change of design variables for design improvement. The second is, so called one-dimensional search, to determine the movement of design variables in the search direction. This basic process is repeated until it approaches to an optimal shape.

In one-dimensional search an accurate and efficient flow solver is indispensable for the computation of pressure distribution and aerodynamic load coefficients such as lift, drag, and pitching moment, which are used in an objective function to be either minimized or maximized. Especially for high-lift design optimization, it is known that the unsteady, time-accurate computation is required for the accurate computation of the flow over a high-lift device at a higher angle of attack close to stall angle where massive flow separation might occur.[1] So far, most of previous studies on high-lift design optimization using the Navier–Stokes equations were based on steady-state computations.[2,3] With regard to this aspect, one of the major interests in the present study is an application of the unsteady approach proposed here to high-lift design optimization to demonstrate its capability not only to delay stall phenomena but also to improve maximum lift performance.

In determining the search direction, the gradients of design variables were traditionally calculated by the finite difference method. It is, however, too expensive to compute the flowfield iteratively with incremented values of a design variable for complex two-dimensional or three-dimensional problems. In addition, this method is so sensitive to the step size of a design variable that it sometimes provides inaccurate signs or sensitivity derivatives.[4,5] Therefore, more robust techniques have been proposed using direct differentiation methods and adjoint variable methods.[4–13] Direct differentiation methods provide computed derivatives, which are coincident with finite differenced derivatives, and are useful when the number of design variable is smaller than that of the objective function and constraints. On the other hand, adjoint variable methods are more advantageous for their capability to compute the gradients of the objective function and constraints when the number of design variable is much larger than that of the objective function and constraints. Adjoint variable methods adopt the formulation of the gradient in either a discrete or a continuous approach. In the discrete approach, which is used in the present work, discretized governing equations are differentiated with respect to design variables, whereas adjoint equations are first differentiated and then discretized in the continuous approach.[10,11]

It is required to incorporate the effect of turbulence as accurately as possible in differentiating the governing equations to deal with critical flows involving strong shocks and flow separations, such as transonic flows with a strong shock and high-angle-of-attack flows close to stall. It is, however, difficult to fully hand differentiate the governing equations including the viscous terms and turbulence terms. Some software tools such as automatic differentiation[8,9,12] are used for the Navier–Stokes equations with a turbulence model. However, this approach is generally less efficient, in terms of computing time and memory overhead, than hand-differentiation codes.[8,13] In the present work the Navier–Stokes equations coupled with two-equation turbulence models are fully differentiated by human hand. Because the $k-\omega$ supersonic transport (SST) model[14,15] shows a better prediction for stall phenomena among popular two-equation turbulence models, the $k-\omega$ SST model is mainly used and then compared with the original $k-\omega$ model[16,17] and the standard $k-\varepsilon$ model.[15] Like the mean flow equations, the turbulence model equations are also hand differentiated to compute accurately the sensitivity derivatives of flow quantities with respect to design variables.

Adjoint variable methods with a usual assumption of constant turbulent eddy-viscosity assumption have been applied to actual aerodynamic design optimizations.[10,11] Also the accuracy of this assumption was reported in Refs. 4 and 5. An aerodynamic sensitivity analysis for the Navier–Stokes equations coupled with two-equation turbulence models was performed on the chimera overlaid grids in Ref. 5, which presents the effects of the constant eddy viscosity

Presented as Paper 2002-0262 at the AIAA 40th Aerospace Sciences Meeting and Exhibit, Reno, NV, 14 January 2003; received 15 March 2003; revision received 5 September 2003; accepted for publication 5 September 2003.

*Research Associate, Department of Aerospace Engineering; currently RIACS Postdoctorial, NASA Ames Research Center. Member AIAA.
†Assistant Professor, Department of Aerospace Engineering. Member AIAA.
‡Professor, Department of Aerospace Engineering. Associate Fellow AIAA.

assumption on sensitivity gradients with respect to several geometric and flow design variables. In the present study all of the design variables that are actually imposed on design optimization are examined using the CSAAV2D code.[5] In addition, both transonic and high-lift design optimizations using the constant eddy-viscosity assumption are rigorously assessed in terms of design accuracy, computer memory requirements, and total design time in various design examples: subsonic and transonic designs for drag minimization and lift maximization and high-lift designs for lift-to-drag-ratio maximization and even $Cl_{\max}$ improvement. Especially in the high-lift design optimization, for the accurate computation of the flow at higher angles of attack very close to stall both flow analysis and sensitivity analysis are performed in an unsteady, time-accurate mode by adopting the dual time-stepping method.

Numerical Background

Flow Analysis

The compressible flow analysis Navier–Stokes solver (CFANS2D), which has been well verified in many applications,[1,5,18] is used for the computation of turbulent viscous flows over single- and multi-element airfoils. The governing equations are the two-dimensional, unsteady, compressible Navier–Stokes equations coupled with two-equation turbulence models: the $k-\omega$ SST model,[14,15] the $k-\omega$ model,[16,17] and the standard $k-\varepsilon$ model.[15] The governing equations are transformed in generalized coordinates and are solved with a finite volume method. Using a backward Euler implicit method and the dual time-stepping method, the governing equations are discretized in time and linearized in delta form as

$$\left[\frac{I}{J\Delta\tau}+\left(\frac{\partial \boldsymbol{R}_s}{\partial \boldsymbol{Q}}+\frac{\partial \boldsymbol{S}}{\partial \boldsymbol{Q}}\right)^{n+1,m}\right]\Delta \boldsymbol{Q}^{n+1,m+1}$$

$$=-\{\boldsymbol{R}_s+\boldsymbol{S}\}^{n+1,m}=-\boldsymbol{R}^{n+1,m}$$

$$\boldsymbol{S}^{n+1}=\frac{1.5\boldsymbol{Q}^{n+1}-2\boldsymbol{Q}^{n}+0.5\boldsymbol{Q}^{n-1}}{J\Delta t} \tag{1}$$

where J is the Jacobian of transformation, τ and superscript m represent pseudotime while t and n for physical time. $\boldsymbol{R}_s$ and $\boldsymbol{S}$ are the residual of the steady-state flow equations and unsteady source-like term, respectively. $\boldsymbol{Q}$ is the six-element vector of conservative variables $(\rho, \rho u, \rho v, \rho E, \rho k, \rho\omega)^T$.

For the calculation of the residual, convective terms are upwind differenced based on Roe's flux-difference-splitting (FDS) scheme[19] and viscous terms are central-differenced. A MUSCL (monotone upstream-centered scheme for conservation laws) approach using a third-order interpolation is used to obtain a higher order of spatial accuracy.[20] The third order of spatial accuracy is kept in all calculations. For a temporal integration the LU-SGS scheme by Yoon and Colleagues[21,22] is adopted to efficiently solve Eq. (1). Wall boundary conditions are applied explicitly with the nonslip condition. For inflow and outflow boundaries characteristic conditions based on one-dimensional Riemann invariants are imposed. For the chimera grid scheme a bilinear interpolation that was known to be robust and easy to implement is adopted for the hole-cutting boundary.[1,18]

Unsteady Sensitivity Analysis

In this section an unsteady sensitivity analysis method based on an unsteady, time-accurate flow analysis is presented. The discrete residual of the unsteady flow equations derived in Eq. (1) can be written as

$$\{\boldsymbol{R}\}=\{\boldsymbol{R}_s\}+\{\boldsymbol{S}\}=\boldsymbol{R}\{\boldsymbol{Q},\boldsymbol{X},\boldsymbol{D}\}=\{0\} \tag{2}$$

where $\boldsymbol{X}$ is the computational grid position and $\boldsymbol{D}$ is the vector of design variables. Similarly, the vector of the aerodynamic objective function F to be either minimized or maximized is also dependent on $\boldsymbol{Q}$, $\boldsymbol{X}$, and $\boldsymbol{D}$ as

$$\{F\}=\{F(\boldsymbol{Q},\boldsymbol{X},\boldsymbol{D})\} \tag{3}$$

Sensitivity derivatives of the aerodynamic functions are calculated by directly differentiating Eqs. (2) and (3) with respect to $\boldsymbol{D}$ as

$$\left\{\frac{\mathrm{d}\boldsymbol{R}}{\mathrm{d}\boldsymbol{D}}\right\}=\left[\frac{\partial \boldsymbol{R}}{\partial \boldsymbol{Q}}\right]\left\{\frac{\mathrm{d}\boldsymbol{Q}}{\mathrm{d}\boldsymbol{D}}\right\}+\left[\frac{\partial \boldsymbol{R}}{\partial \boldsymbol{X}}\right]\left\{\frac{\mathrm{d}\boldsymbol{X}}{\mathrm{d}\boldsymbol{D}}\right\}+\left\{\frac{\partial \boldsymbol{R}}{\partial \boldsymbol{D}}\right\}=\{0\} \tag{4}$$

$$\left\{\frac{\mathrm{d}F}{\mathrm{d}\boldsymbol{D}}\right\}=\left[\frac{\partial F}{\partial \boldsymbol{Q}}\right]^T\left\{\frac{\mathrm{d}\boldsymbol{Q}}{\mathrm{d}\boldsymbol{D}}\right\}+\left[\frac{\partial F}{\partial \boldsymbol{X}}\right]^T\left\{\frac{\mathrm{d}\boldsymbol{X}}{\mathrm{d}\boldsymbol{D}}\right\}+\left\{\frac{\partial F}{\partial \boldsymbol{D}}\right\} \tag{5}$$

In the adjoint-variable (AV) method the sensitivity derivatives of the aerodynamic functions are obtained by combining Eqs. (4) and (5) as

$$\left\{\frac{\mathrm{d}F}{\mathrm{d}\boldsymbol{D}}\right\}=\left\{\frac{\partial F}{\partial \boldsymbol{Q}}\right\}^T\left\{\frac{\mathrm{d}\boldsymbol{Q}}{\mathrm{d}\boldsymbol{D}}\right\}+\left\{\frac{\partial F}{\partial \boldsymbol{X}}\right\}^T\left\{\frac{\mathrm{d}\boldsymbol{X}}{\mathrm{d}\boldsymbol{D}}\right\}+\left\{\frac{\partial F}{\partial \boldsymbol{D}}\right\}$$
$$+\boldsymbol{\Lambda}^T\left(\left[\frac{\partial \boldsymbol{R}}{\partial \boldsymbol{Q}}\right]\left\{\frac{\mathrm{d}\boldsymbol{Q}}{\mathrm{d}\boldsymbol{D}}\right\}+\left[\frac{\partial \boldsymbol{R}}{\partial \boldsymbol{X}}\right]\left\{\frac{\mathrm{d}\boldsymbol{X}}{\mathrm{d}\boldsymbol{D}}\right\}+\left\{\frac{\partial \boldsymbol{R}}{\partial \boldsymbol{D}}\right\}\right) \tag{6}$$

where $\boldsymbol{\Lambda}$ represents the six-element adjoint vector of Lagrangian multipliers $(\lambda_1, \lambda_2, \lambda_3, \lambda_4, \lambda_5, \lambda_6)^T$ corresponding to the conservative variables $(\rho, \rho u, \rho v, \rho E, \rho k, \rho\omega)^T$. The geometric sensitivity vector $\{\mathrm{d}\boldsymbol{X}/\mathrm{d}\boldsymbol{D}\}$ can be calculated by differentiating the grid-generation code. In the present work finite difference approximation is applied for simplicity. Rearranging Eq. (6) yields the following equation:

$$\left\{\frac{\mathrm{d}F}{\mathrm{d}\boldsymbol{D}}\right\}=\left\{\frac{\partial F}{\partial \boldsymbol{X}}\right\}^T\left\{\frac{\mathrm{d}\boldsymbol{X}}{\mathrm{d}\boldsymbol{D}}\right\}+\left\{\frac{\partial F}{\partial \boldsymbol{D}}\right\}+\boldsymbol{\Lambda}^T\left(\left[\frac{\partial \boldsymbol{R}}{\partial \boldsymbol{X}}\right]\left\{\frac{\mathrm{d}\boldsymbol{X}}{\mathrm{d}\boldsymbol{D}}\right\}\right.$$
$$\left.+\left\{\frac{\partial \boldsymbol{R}}{\partial \boldsymbol{D}}\right\}\right)+\left(\left\{\frac{\partial F}{\partial \boldsymbol{Q}}\right\}^T+\boldsymbol{\Lambda}^T\left[\frac{\partial \boldsymbol{R}}{\partial \boldsymbol{Q}}\right]\right)\left\{\frac{\mathrm{d}\boldsymbol{Q}}{\mathrm{d}\boldsymbol{D}}\right\} \tag{7}$$

Without evaluating the vector $\{\mathrm{d}\boldsymbol{Q}/\mathrm{d}\boldsymbol{D}\}$, the sensitivity derivatives of the aerodynamic functions can be calculated as

$$\left\{\frac{\mathrm{d}F}{\mathrm{d}\boldsymbol{D}}\right\}=\left\{\frac{\partial F}{\partial \boldsymbol{X}}\right\}^T\left\{\frac{\mathrm{d}\boldsymbol{X}}{\mathrm{d}\boldsymbol{D}}\right\}+\left\{\frac{\partial F}{\partial \boldsymbol{D}}\right\}$$
$$+\boldsymbol{\Lambda}^T\left(\left[\frac{\partial \boldsymbol{R}}{\partial \boldsymbol{X}}\right]\left\{\frac{\mathrm{d}\boldsymbol{X}}{\mathrm{d}\boldsymbol{D}}\right\}+\left\{\frac{\partial \boldsymbol{R}}{\partial \boldsymbol{D}}\right\}\right) \tag{8}$$

if and only if the arbitrary vector $\boldsymbol{\Lambda}$ satisfies the following adjoint equation:

$$\left[\frac{\partial \boldsymbol{R}}{\partial \boldsymbol{Q}}\right]^T\boldsymbol{\Lambda}+\left\{\frac{\partial F}{\partial \boldsymbol{Q}}\right\}=\left(\left[\frac{\partial \boldsymbol{R}_s}{\partial \boldsymbol{Q}}\right]^T+\frac{1.5I}{J\Delta t}\right)\boldsymbol{\Lambda}+\left\{\frac{\partial F}{\partial \boldsymbol{Q}}\right\}=\{0\} \tag{9}$$

To obtain the solution vector $\boldsymbol{\Lambda}$ in Eq. (9), the backward Euler implicit method with pseudotime marching is used as

$$\left(\frac{I}{J\Delta\tau}+\left[\frac{\partial \boldsymbol{R}_s}{\partial \boldsymbol{Q}}\right]^T+\frac{1.5I}{J\Delta t}\right)\Delta\boldsymbol{\Lambda}^{m+1}$$
$$=-\left(\left[\frac{\partial \boldsymbol{R}_s}{\partial \boldsymbol{Q}}\right]^T+\frac{1.5I}{J\Delta t}\right)\boldsymbol{\Lambda}^m-\left\{\frac{\partial F}{\partial \boldsymbol{Q}}\right\}$$

$$\boldsymbol{\Lambda}^{m+1}=\boldsymbol{\Lambda}^m+\Delta\boldsymbol{\Lambda}^{m+1} \tag{10}$$

For efficient calculation of $[\partial \boldsymbol{R}_s/\partial \boldsymbol{Q}]^T$, the residual vector $[\partial \boldsymbol{R}_s/\partial \boldsymbol{Q}]^T$ is differentiated by the primitive variable vector $\boldsymbol{Q}_p=(\rho, u, v, w, p, k, \omega)^T$ rather than by the conservative variable vector $\boldsymbol{Q}$. Introducing the transformation matrix $M=\partial \boldsymbol{Q}/\partial \boldsymbol{Q}_p$, the transposed flux Jacobian can be calculated by

$$\left[\frac{\partial \boldsymbol{R}_s}{\partial \boldsymbol{Q}}\right]^T=\left(\left[\frac{\partial \boldsymbol{R}_s}{\partial \boldsymbol{Q}_p}\right]\left[\frac{\partial \boldsymbol{Q}_p}{\partial \boldsymbol{Q}}\right]\right)^T=\left[\frac{\partial \boldsymbol{Q}_p}{\partial \boldsymbol{Q}}\right]^T\left[\frac{\partial \boldsymbol{R}_s}{\partial \boldsymbol{Q}_p}\right]^T$$
$$=M^{-1^T}\left[\frac{\partial \boldsymbol{R}_s}{\partial \boldsymbol{Q}_p}\right]^T \tag{11}$$

The inverse transformation matrix in transposed form is given as

$$M^{-1^T} = \begin{bmatrix} 1 & -u/\rho & -v/\rho & \dfrac{(\gamma-1)\{u^2+v^2\}}{2} & -k/\rho & -\omega/\rho \\ 0 & 1/\rho & 0 & -(\gamma-1)u & 0 & 0 \\ 0 & 0 & 1/\rho & -(\gamma-1)v & 0 & 0 \\ 0 & 0 & 0 & (\gamma-1) & 0 & 0 \\ 0 & 0 & 0 & 0 & 1/\rho & 0 \\ 0 & 0 & 0 & 0 & 0 & 1/\rho \end{bmatrix} \tag{12}$$

For steady-state computations unsteady time terms in the preceding equations can be vanished by setting the physical time step Δt to infinity. Boundary conditions in the AV methods are given from Eq. (9) as

$$\left(\left[\frac{\partial \boldsymbol{R}_s}{\partial \boldsymbol{Q}}\right]^T + \frac{1.5I}{J\Delta t}\right)\boldsymbol{\Lambda} + \left[\frac{\partial \boldsymbol{R}_{sB}}{\partial \boldsymbol{Q}}\right]^T \boldsymbol{\Lambda}_B + \left\{\frac{\partial F}{\partial \boldsymbol{Q}}\right\} = \{0\} \tag{13a}$$

$$\left[\frac{\partial \boldsymbol{R}_s}{\partial \boldsymbol{Q}_B}\right]^T \boldsymbol{\Lambda} + \left(\left[\frac{\partial \boldsymbol{R}_{sB}}{\partial \boldsymbol{Q}_B}\right]^T + \frac{1.5I}{J\Delta t}\right)\boldsymbol{\Lambda}_B + \left\{\frac{\partial F}{\partial \boldsymbol{Q}_B}\right\} = \{0\} \tag{13b}$$

where subscript B represents boundary cells.

For the chimera grid scheme a bilinear interpolation is adopted for the hole-cutting boundary. These boundary conditions also need to be carefully treated. The discrete residuals at the fringe cells of the main grid and the subgrid can be written as

$$\left\{\boldsymbol{R}_F^M\right\} = \left\{\boldsymbol{R}_{sF}^M\right\} + \left\{\boldsymbol{S}_F^M\right\} = \left\{\boldsymbol{R}_F^M\left(\boldsymbol{Q}_F^M, \boldsymbol{Q}^S\right)\right\} = \{0\} \tag{14a}$$

$$\left\{\boldsymbol{R}_F^S\right\} = \left\{\boldsymbol{R}_{sF}^S\right\} + \left\{\boldsymbol{S}_F^S\right\} = \left\{\boldsymbol{R}_F^S\left(\boldsymbol{Q}_F^S, \boldsymbol{Q}^M\right)\right\} = \{0\} \tag{14b}$$

where the subscript F represents fringe cells and the superscripts M and S represent the main grid and subgrid domain, respectively. Then the equations for boundary conditions at fringe cells can be derived from the Eqs. (9) and (14) as

$$\left(\left[\frac{\partial \boldsymbol{R}_s^M}{\partial \boldsymbol{Q}^M}\right]^T + \frac{1.5I}{J\Delta t}\right)\boldsymbol{\Lambda}^M + \left[\frac{\partial \boldsymbol{R}_{sF}^S}{\partial \boldsymbol{Q}^M}\right]^T \boldsymbol{\Lambda}_F^S + \left\{\frac{\partial F^M}{\partial \boldsymbol{Q}^M}\right\} = \{0\} \tag{15a}$$

$$\left(\left[\frac{\partial \boldsymbol{R}_s^S}{\partial \boldsymbol{Q}^S}\right]^T + \frac{1.5I}{J\Delta t}\right)\boldsymbol{\Lambda}^S + \left[\frac{\partial \boldsymbol{R}_{sF}^M}{\partial \boldsymbol{Q}^S}\right]^T \boldsymbol{\Lambda}_F^M + \left\{\frac{\partial F^S}{\partial \boldsymbol{Q}^S}\right\} = \{0\} \tag{15b}$$

$$\left[\frac{\partial \boldsymbol{R}_s^M}{\partial \boldsymbol{Q}_F^M}\right]^T \boldsymbol{\Lambda}^M + \left(\left[\frac{\partial \boldsymbol{R}_{sF}^M}{\partial \boldsymbol{Q}_F^M}\right]^T + \frac{1.5I}{J\Delta t}\right)\boldsymbol{\Lambda}_F^M + \left\{\frac{\partial F^M}{\partial \boldsymbol{Q}_F^M}\right\} = \{0\} \tag{15c}$$

$$\left[\frac{\partial \boldsymbol{R}_s^S}{\partial \boldsymbol{Q}_F^S}\right]^T \boldsymbol{\Lambda}^S + \left(\left[\frac{\partial \boldsymbol{R}_{sF}^S}{\partial \boldsymbol{Q}_F^S}\right]^T + \frac{1.5I}{J\Delta t}\right)\boldsymbol{\Lambda}_F^S + \left\{\frac{\partial F^S}{\partial \boldsymbol{Q}_F^S}\right\} = \{0\} \tag{15d}$$

In the step of an unsteady sensitivity analysis, the main difficulty lies in the differentiation of a one- or two-equation turbulence model because of complicated terms such as turbulence production and dissipation terms. To reduce the effort to differentiate the turbulence transport equations, the turbulent eddy viscosity μ_T is usually assumed to be constant in the adjoint variable methods.[10,11] That is, the derivatives of μ_T with respect to the conservative variables $\boldsymbol{Q}$ are set to zero. Because $\mathrm{d}\mu_T/\mathrm{d}\boldsymbol{Q}$ is a very large banded matrix of six conservative variables at eight node cells as shown in Fig. 1, it requires quite an amount of computer memory. The constant eddy-viscosity assumption saves computing time as well as memory overhead by avoiding the need to solve the differentiated turbulence equations. This assumption, however, might not guarantee the required accuracy of the derivatives because it neglects the contribution of the turbulence model to the flow analysis,[4,5] which can directly influence on the design of optimal aerodynamic shape.

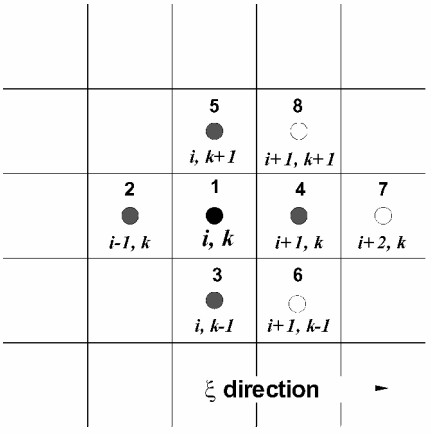

Fig. 1 Grid cells required for $\mathrm{d}\mu_T/\mathrm{d}Q$ calculation.

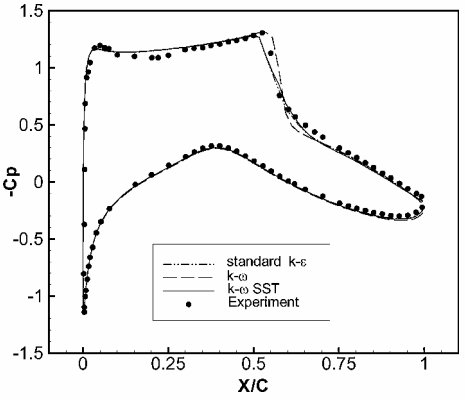

Fig. 2 Surface-pressure coefficients over the RAE 2822 airfoil at $\alpha = 2.79$ deg, $M = 0.73$, and $Re = 6.5 \times 10^6$.

Results and Discussion

Flow Analysis

Both single- and multi-element airfoils are tested for the validation of the parallelized CFANS2D flow solver.[1] For the case of single airfoil, the transonic flow over the Royal Aircraft Establishment (RAE) 2822 airfoil is computed at a Mach number of 0.73, a Reynolds number of 6.5×10^6, and an angle of attack 2.79 deg. A 129×65 hyperbolic grid is used with the wall spacing of 1×10^{-5} chord. The computed surface pressure coefficients from the flow solver using the $k-\omega$ SST model[14,15] are compared with those from the $k-\omega$ model,[16,17] the standard $k-\varepsilon$ model,[15] and the experimental data[23] in Fig. 2.

In case of multi-element airfoil, the flow over the National Aerospace Laboratory (NLR) 7301 airfoil with a 32%c flap is tested at a Mach number of 0.185, a Reynolds number of 2.51×10^6, and an angle of attack of 13.1 deg. The flap is positioned with a deflection angle of 20 deg, an overhang of 5.3%c, and a gap of 2.6%c. A 249×81 hyperbolic grid for the basic airfoil and a 125×41 grid for the flap are used with the wall spacing on the order of 10^{-6} chord in a chimera overlaid grid system. For accurate prediction for higher angles of attack over 13.1 deg, computations are performed in a time-accurate, unsteady manner using the dual time-stepping method as already verified in the previous study.[1] The computed surface-pressure coefficients using two-equation turbulence models are compared with the experimental data[24] in Fig. 3. Three computed results from different turbulence models show quite a good agreement with experiments. Figure 4 shows lift coefficients at the wide range of angles of attack from zero to maximum lift. Overall, the computed result using the $k-\omega$ SST model yields slightly higher predictions of lift coefficient. Especially, the capability of the present flow solver to predict the stall angle of 14.1 deg precisely is noted, which is crucial in finding $Cl_{\max}$ during the actual high-lift design optimization.

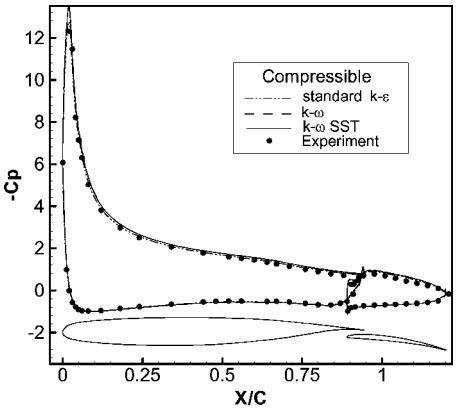

Fig. 3 Surface-pressure coefficients over the NLR 7301 airfoil with flap at $\alpha = 13.1$ deg, $M = 0.185$, and $Re = 2.51 \times 10^6$.

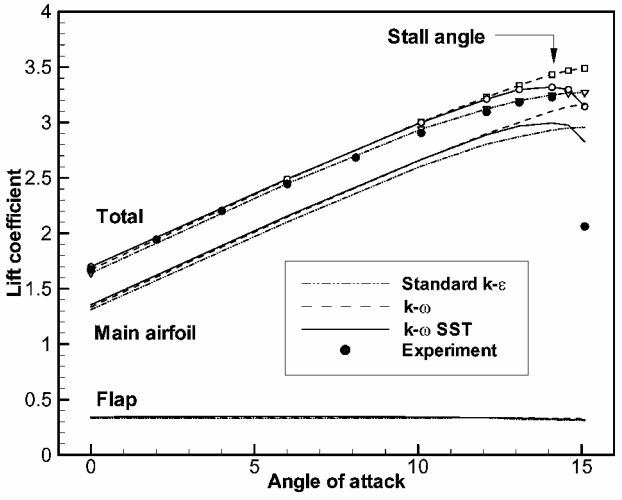

Fig. 4 Lift coefficient vs angle of attack for the NLR 7301 airfoil with flap.

Effects on Sensitivity Analysis

To examine the effects of constant eddy viscosity (CEV) assumption more closely than the previous study,[5] all of the sensitivity gradients of design variables computed from the CEV assumption are compared with those from the variable eddy viscosity (VEV) assumption for three different flow regimes: subsonic and transonic turbulent flows over the RAE 2822 airfoil and a low-speed turbulent flow over the NLR 7301 with flap at a high angle of attack close to stall angle. In addition, sensitivity gradients of an objective function with respect to design variables computed from the $k-\omega$ SST model are compared with those from the $k-\omega$ model and the standard $k-\varepsilon$ model to study the effects of turbulence model under the CEV assumption.

Transonic Airfoil with a Strong Shock

To examine the effects of shock discontinuity on sensitivity gradients, the RAE 2822 transonic airfoil is tested at a Reynolds number of 6.5×10^6, an angle of attack of 2.79 deg, and a freestream Mach number of 0.73, where a strong shock wave appears on the upper airfoil surface. The objective is to maximize lift coefficient. Angle of attack α is given as a flow design variable, and 20 geometric design variables are also given on both the upper and lower airfoil surfaces using 10 Hicks–Henne functions,[25] respectively. Figure 5 shows clearly that the CEV assumption can lead to serious deviations in obtaining the sensitivity gradients of lift coefficient in turbulent flows involving a strong shock. For the design variable of angle of attack, the deviation reaches up to about 50%, and the maximum deviation is as much as 250% for geometric design variables. Because the gradient of flow quantities on the upper airfoil surface is much larger than the lower surface, the CEV assumption shows quite a difference mostly on the upper surface. The third order of magnitude of the initial residual is enough for the convergence criteria in both the AV codes with/without the CEV assumption. However, for the purpose of careful comparison, the convergence criterion is set to the fourth order of magnitude of the initial residual in all computations.

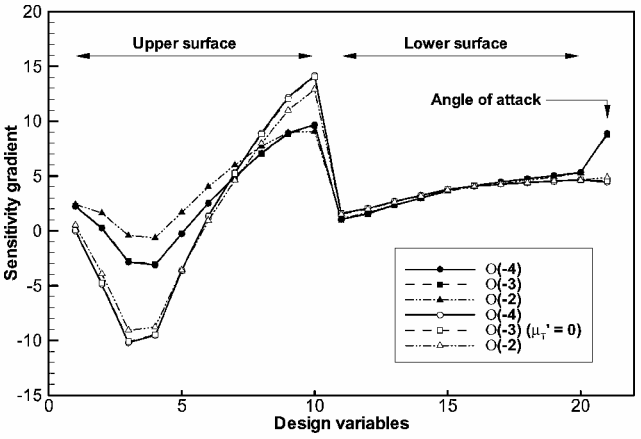

Fig. 5 Convergence of sensitivity gradients of lift coefficient at $M = 0.73$: $k-\omega$ SST model.

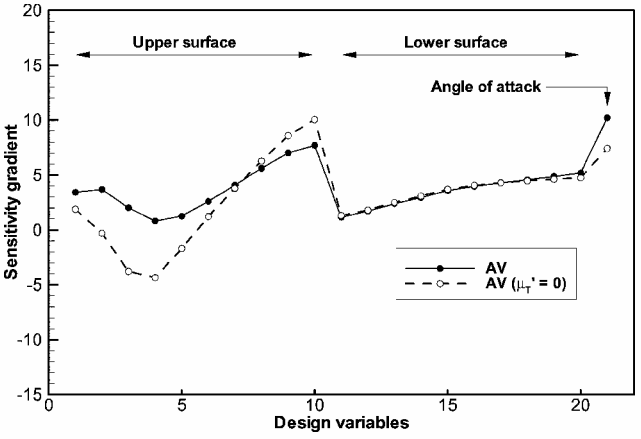

Fig. 6 Sensitivity gradients of lift coefficient at $M = 0.73$: $k-\varepsilon$ model.

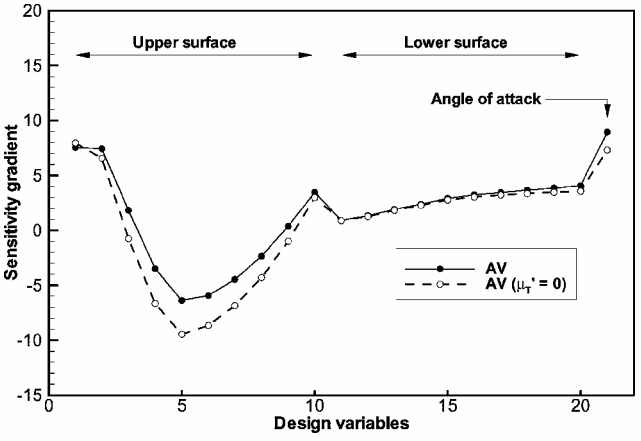

Fig. 7 Sensitivity gradients of lift coefficient at $M = 0.73$: $k-\omega$ model.

Effects of Turbulence Models

Three different two-equation turbulence models are tested to examine the effects of turbulence models on sensitivity gradients. Much like the $k-\omega$ SST model, the standard $k-\varepsilon$ and the $k-\omega$ model also show a similar behavior in predicting sensitivity gradients as shown in Figs. 6 and 7. It is known that the CEV assumption might yield inaccurate sensitivity gradients because it neglects the

very large value of the turbulent eddy-viscosity derivative, especially in the downstream adverse pressure gradient region after the shock wave, which directly affects the variation of aerodynamic load coefficients.[4,5] However, this issue on the CEV assumption is still considered moot in actual design applications.

Subsonic Turbulent Airfoil

In this case the RAE 2822 airfoil is tested again at a freestream Mach number of 0.63, a Reynolds number of 6.5×10^6, and an angle of attack of 2.79 deg, where a strong shock does not appear on the airfoil surface. The objective is to maximize lift to drag ratio C_l/C_d. Sensitivity gradients with the CEV assumption show a little difference from the complete AV code of VEV assumption, as shown in Fig. 8. For geometric design variables the maximum deviation of 51% occurs near suction peak on the upper surface, whereas the deviation is less than 2% for the design variable of angle of attack. Contrary to the transonic case involving a strong shock, the AV code with the CEV assumption shows very mild deviations.

Multi-Element Airfoil Close to Stall

To demonstrate the capability of the AV code to treat complex geometry, the flow over the NLR 7301 airfoil with a 32%c flap is tested on a chimera overlaid grid at a Mach number of 0.185, a Reynolds number of 2.51×10^6, and an angle of attack of 13.1 deg, which is very close to the stall angle of 14.1 deg. As mentioned earlier, the flow information is previously obtained from unsteady computations in a time-accurate manner using the dual time-stepping method. Sensitivity gradients of lift coefficient with respect to angle of attack and geometric changes of the main airfoil and flap are compared in Fig. 9. For the design variable of angle of attack, the deviation is 40%, and the maximum deviations reach up to 43 and 20% on the upper surfaces of the main airfoil and flap, respectively.

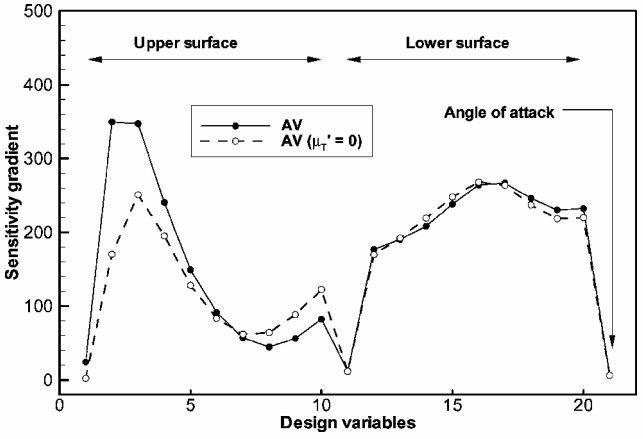

Fig. 8 Sensitivity gradients of lift to drag ratio at $M = 0.63$: $k - \omega$ SST model.

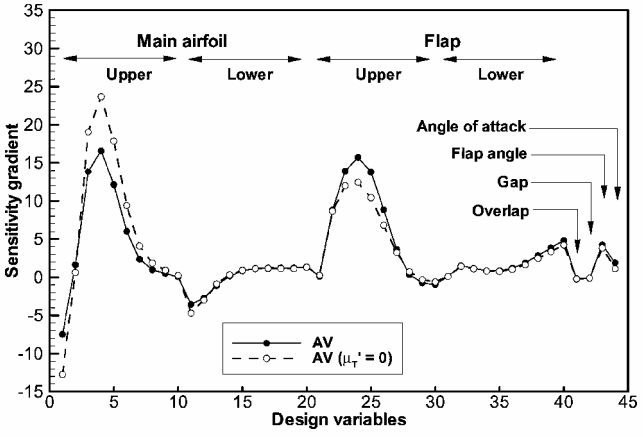

Fig. 9 Sensitivity gradients of lift coefficient at $M = 0.185$: NLR 7301 airfoil with flap.

Table 1 Comparison of computing time and memory requirement

Design	VEV	CEV
Single		
CPU time	1.0	0.61
Memory	1.0	0.36
Multi		
CPU time	1.0	0.57
Memory	1.0	0.35

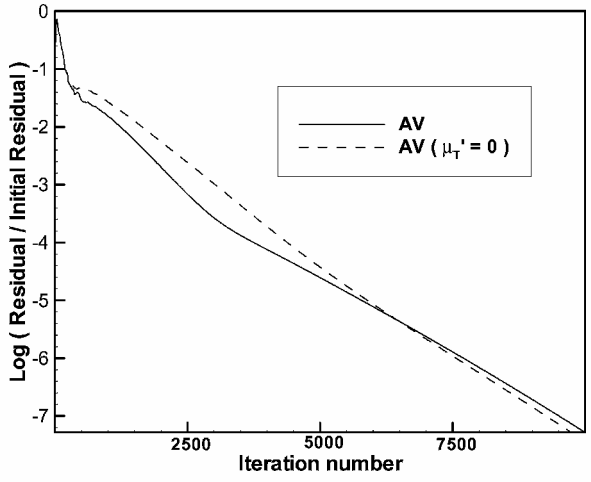

Fig. 10 Comparison of convergence histories.

Computing Time and Memory Requirements

The convergence property of the AV code with the VEV assumption is roughly the same as that of the AV code with the CEV assumption as shown in Fig. 10. Even though residual histories are shown up to over seventh order of magnitude of the initial residual, the third or fourth order of magnitude is enough for the convergence criterion of sensitivity analysis in actual design examples. Computing time and memory requirements of the AV code with the CEV assumption are compared to those of the AV code with the VEV assumption in Table 1. The CEV assumption reduces the CPU time and computer memory overheads by about 40 and 65%, respectively. In an engineering sense it would be considerably efficient to implement this assumption into actual design optimization if design results are acceptable, which will be examined in the next design examples.

Effects on Transonic Design Optimization

The two-dimensional compressible flow analysis Navier–Stokes (CFANS2D) solver[1] and two-dimensional compressible sensitivity analysis adjoint variables (CSAAV2D) code[5] are used for single airfoil design optimization according to the design procedure in Fig. 11. Optimization is performed using the Broydon–Fletcher–Goldfarb–Shanno (BFGS) variable metric method supported by the Design Optimization Tool (DOT) commercial software.[26] Twenty geometric design variables are given on the upper and lower airfoil surfaces.

To examine the effects of the CEV assumption on shock discontinuity, the RAE 2822 transonic airfoil is chosen as a baseline model and tested at two different Mach numbers of 0.73 and 0.63, respectively with/without a strong shock wave. In all design examples convergence criteria for the flow solver and sensitivity analysis code are set to the fourth and third order of magnitude of the initial residual, respectively.

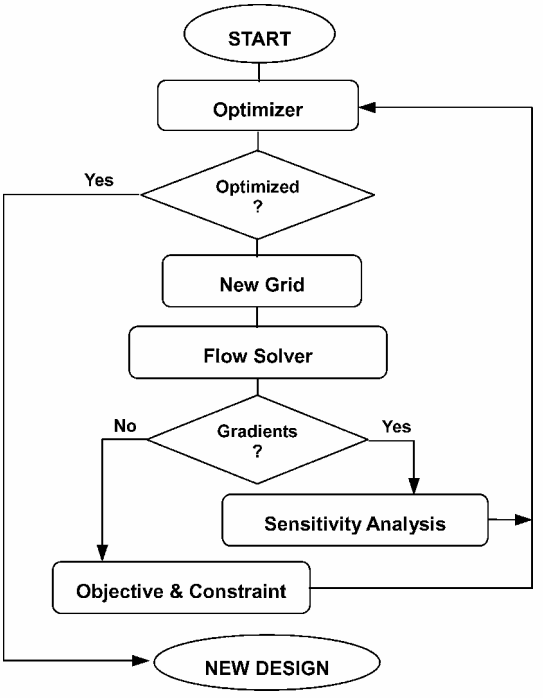

Fig. 11 Flowchart of a gradient-based design optimization.

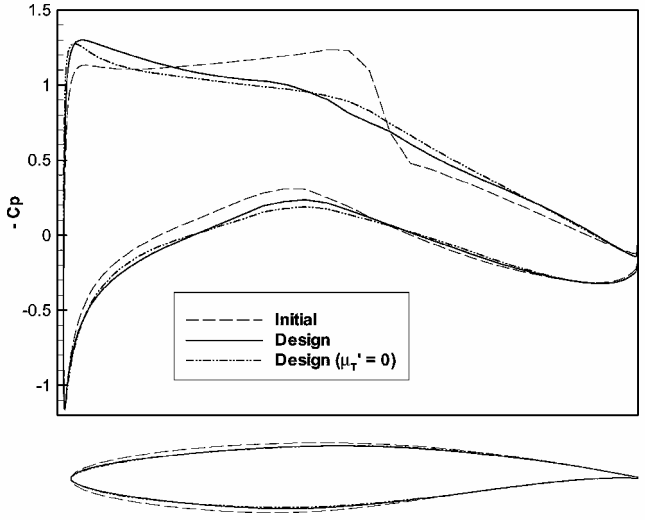

Fig. 12 Drag minimization with lift constraint for single airfoil at $M = 0.73$.

Drag Minimization with Lift Constraint

The RAE 2822 transonic airfoil is adopted as a baseline model and redesigned at a Mach number of 0.73, a Reynolds number of 6.5×10^6, and a fixed angle of attack of 2.79 deg. The objective of the first example is to minimize drag coefficient with lift constraint. To perform the sensitivity analysis to obtain lift and drag coefficients simultaneously, the objective function to be minimized is given by the following equation:

$$F = Cd + \omega \times \max(Cl - Cl_0, 0.0) \tag{16}$$

where Cl_0 is the target lift coefficient and ω is a weighting value. The initial and designed surface pressure coefficients are compared in Fig. 12. After 14 design iterations the drag coefficient is reduced from 0.01876 to 0.01341 keeping the target lift coefficient at a threshold value of 0.8 as shown in Fig. 13. Even though it might be defined arbitrarily by a designer's choice, the same design convergence criterion is imposed fairly on both the VEV and CEV design examples. The VEV design case calls the flow solver

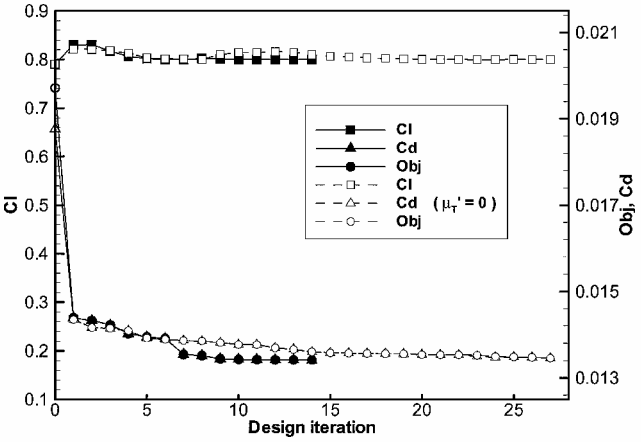

Fig. 13 Design progress of drag minimization with lift constraint at $M = 0.73$.

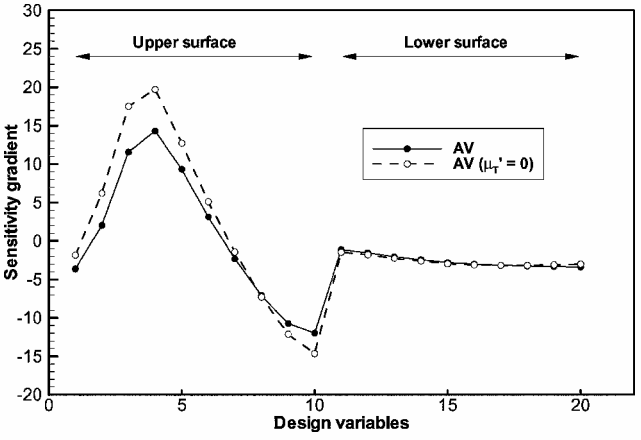

Fig. 14 Sensitivity gradients for drag minimization with lift constraint.

66 times and the sensitivity analysis code 14 times, whereas the CEV design case calls the flow solver 117 times and the sensitivity analysis code 27 times. The CEV design case requires much more design iterations because of the accuracy problem in determining a search direction. However, recalling that the AV code with the CEV assumption yields quite a difference in determining gradients of lift coefficient from the AV code with the VEV assumption as already seen in Fig. 5, it is interesting that the designed drag coefficient using the CEV assumption yields just 2% higher value than that of the VEV design case. This can be explained by the facts that the gradients of the drag coefficient computed from the CEV assumption produce a relatively smaller deviations compared to the case of the lift coefficient as shown in Figs. 5 and 14 and that a shock wave representing nonlinearity in transonic flows has disappeared after the second design iteration. The shock wave causing wave drag on the initial airfoil is disappeared on the final designed airfoil as shown in Fig. 15.

Shock-Wave Clearance

The effects of the CEV assumption on subsonic design without a shock wave are examined by analyzing the flows around the RAE 2822 airfoil as a baseline airfoil at a Mach number of 0.63, a Reynolds number of 6.5×10^6, and a fixed angle of attack of 2.79 deg. The objective is to maximize the lift-to-drag ratio, which is simply given by

$$F = Cl/Cd \tag{17}$$

The designed surface-pressure coefficients and design progress are shown in Figs. 16 and 17. The VEV design improves the lift-to-drag ratio from 57.22 to 64.73 after three design iterations, calling

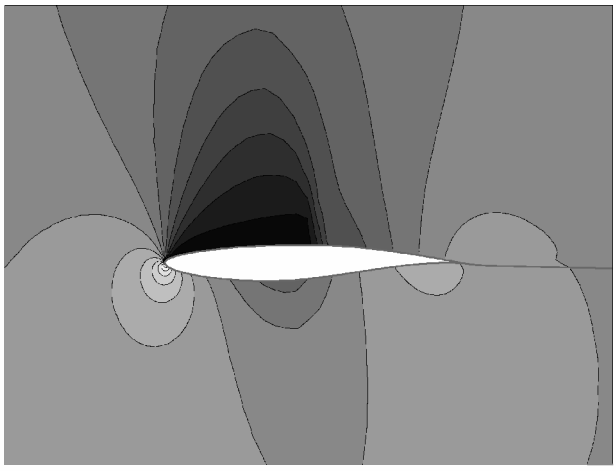

a) Initial airfoil

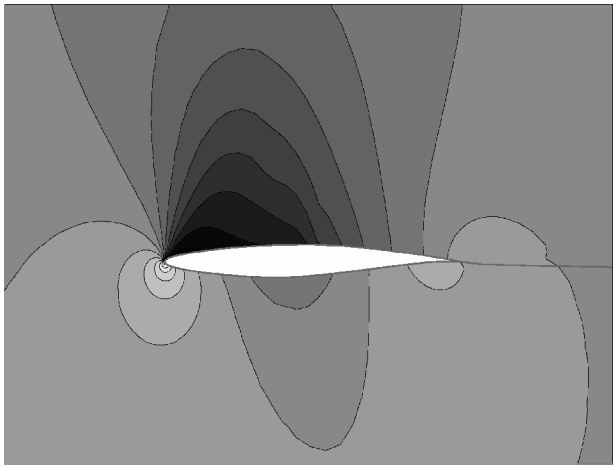

b) Design airfoil

Fig. 15 Comparison of isopressure contours before and after design.

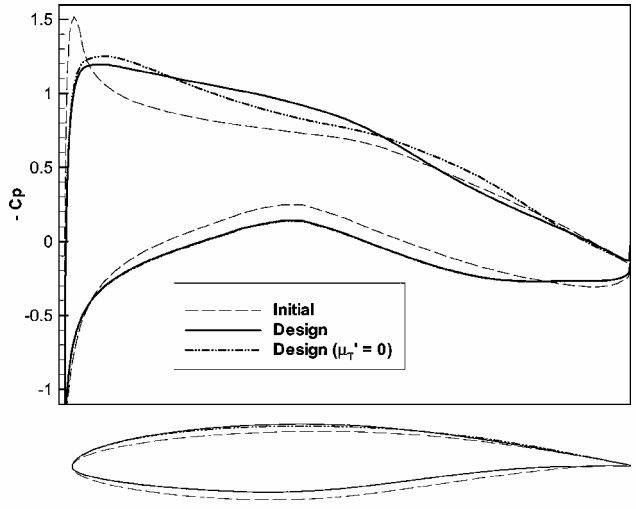

Fig. 16 Lift-to-drag maximization for single airfoil at $M = 0.63$.

the flow solver 21 times and the sensitivity analysis code three times. On the other hand, the CEV design ends only after two design iterations with no further advance. Though the CEV design yields some difference in the distribution of upper surface-pressure coefficients, which is expected from the result of sensitivity gradients of lift to drag ratio in Fig. 10, the optimal value of the objective function agrees well with each other. Thus, it seems to be feasible to apply the CEV assumption to subsonic design optimization at a lower angle of attack.

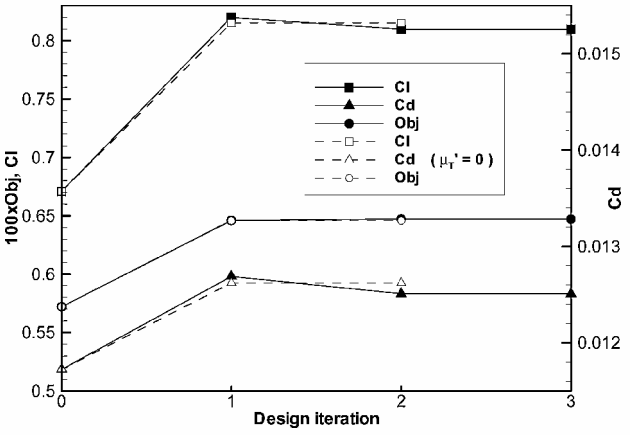

Fig. 17 Design progress of lift-to-drag maximization at $M = 0.63$.

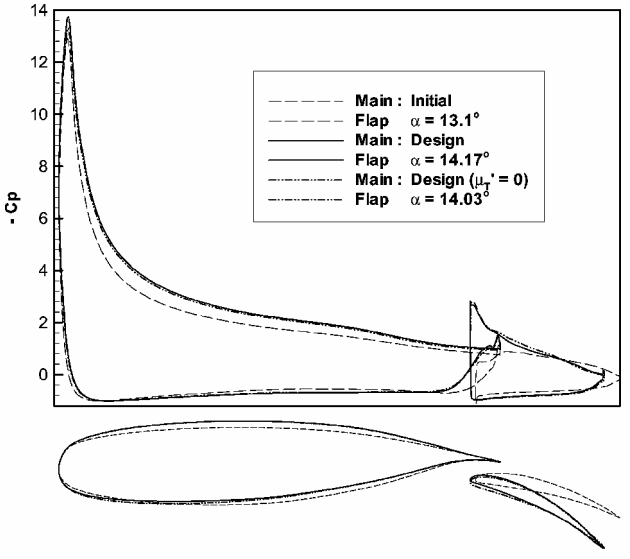

Fig. 18 Improvement of Cl_{max} for multi-element airfoil.

Effects on High-Lift Design Optimization

The essence of high-lift design optimization is undoubtedly to improve Cl_{max} by modifying geometric parameters on each element and by changing the angle of attack as well. In actual high-lift design applications the enhancement of the maximum lift coefficient can cause undesirable lift-to-drag ratios at off-design conditions. In the present study, however, high-lift design examples are restricted to the optimal landing and takeoff configuration at high angles of attack close to the stall angle. For further realistic high-lift design optimization multipoint design optimization would be performed as a future work.

To validate the present design topology based on unsteady sensitivity analysis and chimera overset grid scheme, the NLR 7301 airfoil with flap is tested as a baseline model at a Mach number of 0.185, a Reynolds number of 2.51×10^6, and an angle of attack of 13.1 deg. Among total 44 design variables, a flow design variable of angle of attack and 43 geometric variables are given: 20 design variables on the surfaces of the basic airfoil and flap, respectively, and three geometric changes of flap deflection angle, overlap, and gap. For the accurate prediction of the flowfield very close to stall during the one-dimensional search, flow computations are performed in a time-accurate, unsteady manner using the dual time-stepping method. The effects of the CEV assumption on the multi-element airfoil design optimization are examined in both cases of landing and takeoff configurations at higher angles of attacks close to stall angle.

Maximum-Lift Landing Configuration

The objective of the first example is to maximize the lift coefficient at the floating angle of attack. Thus, the angle of attack is also

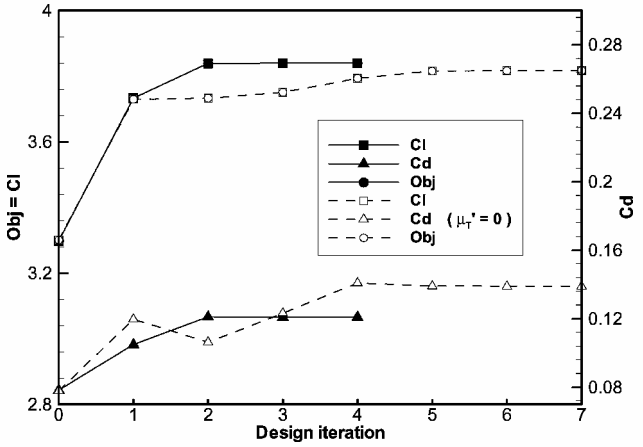

Fig. 19 Design progress of Cl_{max} improvement for multi-element airfoil.

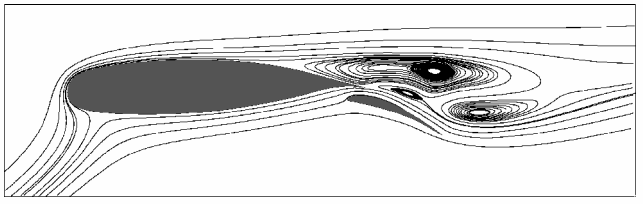

a) Massively separated flow during design

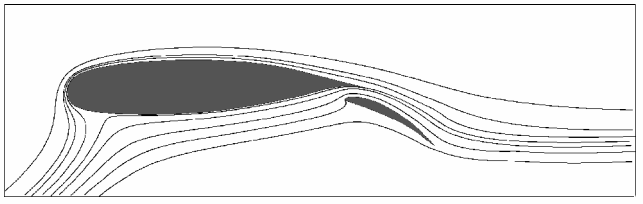

b) Attached flow after design

Fig. 20 Comparison of streamlines over high-lift airfoil with flap.

included as a design variable. The objective function to be maximized is given by Eq. (17). The initial and designed surface-pressure coefficients are compared in Fig. 18. For the design case using the AV code with the VEV assumption, the angle of attack is changed from 13.1 to 14.17 deg, whereas it is changed to 14.03 deg in the CEV design case. Figure 19 shows that the lift coefficients increase from 3.2982 to 3.8399 in the VEV design case and to 3.8171 in the CEV design, respectively. The VEV design calls the flow solver 29 times and the sensitivity analysis code four times, whereas the CEV design calls the flow solver 43 times and the sensitivity analysis code seven times. For a fair comparison the same design convergence criterion is implicitly imposed on both the VEV and CEV design examples. Even though the CEV design requires more design iterations than the VEV design because of the inaccurate information of search direction from the CEV assumption, the designed results show pretty much same configurations in an engineering sense. Figure 20 shows an improvement of Cl_{max} by avoiding a massive-separated flow over a high-lift airfoil using the present design optimization tool.

Takeoff Configuration

The objective of the second example is to maximize the lift-to-drag ratio at a fixed angle of attack of 13.1 deg, where the objective function to be maximized is the lift to drag ratio itself as given in Eq. (17). The distribution of initial and designed surface-pressure coefficients is shown in Fig. 21. After two design iterations the lift-to-drag ratio from the VEV design is increased from 42.35 to 48.39 as in Fig. 22. Likewise, the CEV design shows an improved lift-to-drag ratio of 48.23. Because the initial geometry is originally optimized for takeoff configuration, a noticeable improvement is not

Table 2 Comparison of total design optimization time

Airfoil	Design	Flow solver	AV code	Total
Single	VEV	66×1.0	14×4.8	133.2
	CEV	117×1.0	27×2.9	195.3
Multi	VEV	29×1.0	4×2.0	37.0
	CEV	43×1.0	7×1.2	51.4

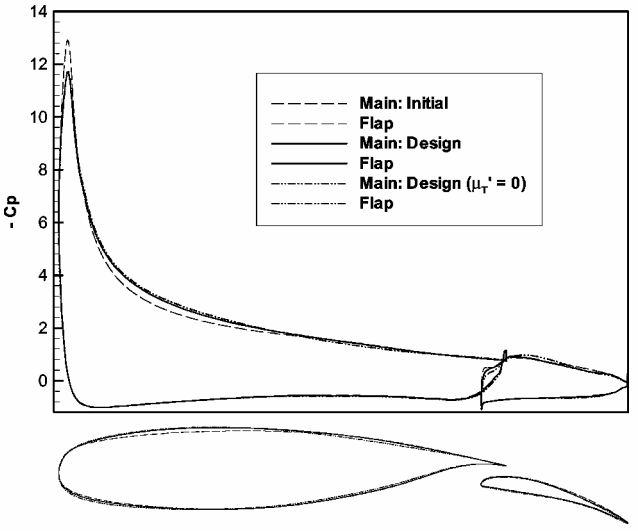

Fig. 21 Lift-to-drag maximization for multi-element airfoil.

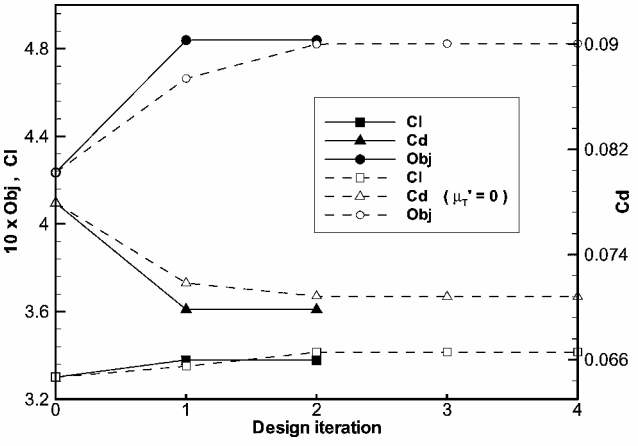

Fig. 22 Design progress of lift-to-drag maximization for multi-element airfoil.

obtained. The high-lift design with the VEV assumption calls flow solver 17 times and sensitivity analysis code two times, whereas the CEV design calls flow solver 29 times and sensitivity analysis code four times.

Total Design Optimization Time

With the same convergence criteria for the flow solver and sensitivity analysis code, total computational cost for design optimization with the CEV assumption is compared to the case of the VEV design by the unit of a flow solver running time as in Table 2. In case of transonic design with a strong shock, the AV code with the VEV assumption takes 4.8 times more than the flow solver, whereas the AV code with the CEV assumption requires 2.9 times. For the drag minimization of a transonic airfoil with the AV code with the VEV assumption, there are 66 flow solver calls and 14 sensitivity code calls, which corresponds to 133 flow solver calls in total. In case of the CEV design, total 195 flow solver calls are required, which results in 45% increase in net computational cost compared to the VEV design case.

In high-lift optimization with the VEV assumption for the Cl_{max} improvement, there are 29 flow solver calls and four AV code calls, which corresponds to total 37 flow solver calls. Much like the transonic design, the high-lift design with the CEV assumption requires about 40% more computing time than the VEV design case. The increase of total computing time in the CEV design is mainly attributed to inaccuracy in determining search direction.

Despite extra computational cost, it seams to be feasible to apply the CEV assumption to actual design applications in general because the design examples using this assumption essentially show comparable results to those of the VEV design.

Conclusions

The effects of a usual assumption of constant turbulent eddy viscosity in an adjoint method on aerodynamic design are carefully investigated in the present study. Accurate steady and unsteady flow analyses are followed by the aerodynamic sensitivity analysis for the Navier–Stokes equations coupled with two-equation turbulence models. For high-lift design optimization at higher angles of attack close to stall, both the flow analysis and sensitivity analysis are performed in an unsteady mode by adopting a dual time-stepping method. The present design tool composed of the unsteady flow solver and the unsteady sensitivity analysis code demonstrates its competency for high-lift design optimization. Through the sensitivity analyses before the actual design process, it is noticed that the CEV assumption can cause inaccurate gradients in the design of the transonic airfoil with a strong shock wave and the multi-element airfoil at a higher angle of attack close to stall. However, the CEV design generally shows a minor difference in obtaining an optimal value of the objective function compared with the VEV design. Therefore, it seems to be feasible to apply this assumption to actual design applications, even to critical problems such as the transonic design with a strong shock wave and the high-lift design at high angles of attack.

Acknowledgment

The present research was supported by the Brain Korea 21 Project. The authors appreciate the financial support.

References

[1]Kim, C. S., Kim, C., and Rho, O. H., "Parallel Computations of High-Lift Airfoil Flows Using Two-Equation Turbulence Models," *AIAA Journal*, Vol. 38, No. 8, 2000, pp. 1360–1368.

[2]Eyi, S., Lee, K. D., Rogers, S. E., and Kwak, D., "High-Lift Design Optimization Using Navier–Stokes Equations," *Journal of Aircraft*, Vol. 33, No. 3, 1996, pp. 499–504.

[3]Kim, S., Alonso, J. J., and Jameson, A., "Two-Dimensional High-Lift Aerodynamic Otimization Using the Continuous Adjoint Method," AIAA Paper 2000-4741, Sept. 2000.

[4]Nielsen, E. J., and Anderson, W. K., "Aerodynamic Design Optimization on Unstructured Meshes Using the Navier–Stokes Equations," AIAA Paper 98-4809, Jan. 1998.

[5]Kim, C. S., Kim, C., and Rho, O. H., "Sensitivity Analysis for the Navier–Stokes Equations with Two-Equation Turbulence Models," *AIAA Journal*, Vol. 39, No. 5, 2001, pp. 838–845.

[6]Nielsen, E. J., and Anderson, W. K., "Recent Improvements in Aerodynamic Design Optimization on Unstructured Meshes," *AIAA Journal*, Vol. 40, No. 6, 2002, pp. 1155–1163.

[7]Eleshaky, M. E., and Baysal, O., "Aerodynamic Shape Optimization Using Sensitivity Analysis on Viscous Flow Equations," *Journal of Fluids Engineering*, Vol. 115, No. 3, 1993, pp. 75–84.

[8]Sherman, L. L., Taylor, A. C., III, Green, L. L., Newman, P. A., Hou, G. J., and Korivi, V. M., "First- and Second-Order Aerodynamic Sensitivity Derivatives via Automatic Differentiation with Incremental Iterative Methods," AIAA Paper 94-4262-CP, Sept. 1994.

[9]Mohammadi, B., "Optimal Shape Design, Reverse Mode of Automatic Differentiation and Turbulence," AIAA Paper 97-0099, Jan. 1997.

[10]Jameson, A., Pierce, N. A., and Martinelli, L., "Optimum Aerodynamic Design Using the Navier–Stokes Equations," AIAA Paper 97-0101, Jan. 1997.

[11]Soemarwoto, B. I., "The Variational Method for Aerodynamic Optimization Using the Navier–Stokes Equations," NASA/CR-97-206277, ICASE Report 97-71, Dec. 1997.

[12]Taylor, A. C., III, and Osolo, A., "Aerodynamic Design Sensitivities by Automatic Differentiation," AIAA Paper 98-2536, June 1998.

[13]Kim, H. J., Kim, C. A., Rho, O. H., and Lee, K. D., "Aerodynamic Sensitivity Analysis for Navier–Stokes Equations," AIAA Paper 99-0402, Jan. 1999.

[14]Menter, F. R., "Influence of Freestream Values on the $k-\omega$ Turbulence Model Predictions," *AIAA Journal*, Vol. 30, No. 6, 1992, pp. 1651–1659.

[15]Menter, F. R., "Two-Equation Eddy-Viscosity Turbulence Models for Engineering Applications," *AIAA Journal*, Vol. 32, No. 8, 1994, pp. 1598–1605.

[16]Wilcox, D. C., "Reassessment of the Scale-Determining Equation for Advanced Turbulence Models," *AIAA Journal*, Vol. 26, No. 11, 1988, pp. 1299–1310.

[17]Wilcox, D. C., "Simulation of Transition with a Two-Equation Turbulence Model," *AIAA Journal*, Vol. 32, No. 2, 1994, pp. 247–255.

[18]Kim, C. S., "Sensitivity Analysis for the Navier–Stokes Equations with Two-Equation Turbulence Models and Its Applications," Ph.D. Dissertation, Dept. of Aerospace Engineering, Seoul National Univ., Republic of Korea, Feb. 2001.

[19]Roe, P. L., "Approximate Riemann Solvers, Parameter Vectors and Difference Schemes," *Journal of Computational Physics*, Vol. 43, 1981, pp. 357–372.

[20]Hwang, S. W., "Numerical Analysis of Unsteady Supersonic Flow over Double Cavity," Ph.D. Dissertation, Dept. of Aerospace Engineering, Seoul National Univ., Republic of Korea, Feb. 1996.

[21]Yoon, S., and Jameson, A., "Lower-Upper Symmetric-Gauss-Seidel Method for the Euler and Navier–Stokes Equations," *AIAA Journal*, Vol. 26, No. 9, 1988, pp. 1025, 1026.

[22]Yoon, S., and Kwak, D., "Three-Dimensional Incompressible Navier–Stokes Solver Using Lower-Upper Symmetric-Gauss-Seidel Algorithm," *AIAA Journal*, Vol. 29, No. 6, 1991, pp. 874, 875.

[23]Cook, P. H., McDonald, M. A., and Firmin, M. C. P., "Aerofoil RAE 2822—Pressure Distributions, and Boundary Layer and Wake Measurements," AGARD, AR 138, May 1979, pp. A6-1–A6-77.

[24]Berg, B. v. d., "Boundary Layer Measurements on a Two-Dimensional Wing with Flap," National Aerospace Lab., TR 79009 U, The Netherlands, Jan. 1979.

[25]Hicks, R. M., and Henne, P. A., "Wing Design by Numerical Optimization," *Journal of Aircraft*, Vol. 15, No. 7, 1978, pp. 407–412.

[26]DOT Users Manual, Ver. 4.00, VMA Engineering, Vanderplaats, Miura and Associate, Inc., 1993.